

The SRG/eROSITA All-Sky Survey

Constraints on $f(R)$ Gravity from Cluster Abundance

E. Artis¹, V. Ghirardini¹, E. Bulbul¹, S. Grandis^{5,2}, C. Garrel¹, N. Clerc³, R. Seppi^{1,7}, J. Comparat¹, M. Cataneo⁴,
Y. E. Bahar¹, F. Balzer¹, I. Chiu⁸, D. Gruen⁵, F. Kleinbreil^{2,4}, M. Kluge¹, S. Krippendorf^{5,6}, X. Li¹⁰, A. Liu¹,
A. Merloni¹, H. Miyatake^{12,13,14}, S. Miyazaki¹¹, K. Nandra¹, N. Okabe⁹, F. Pacaud⁴, P. Predehl¹, M. E. Ramos-Ceja¹,
T. H. Reiprich⁴, J. S. Sanders¹, T. Schrabback^{2,4}, S. Zelmer¹, and X. Zhang¹

¹ Max Planck Institute for Extraterrestrial Physics, Giessenbachstrasse 1, 85748 Garching, Germany

² Universität Innsbruck, Institut für Astro- und Teilchenphysik, Technikerstr. 25/8, 6020 Innsbruck, Austria

³ IRAP, Université de Toulouse, CNRS, UPS, CNES, F-31028 Toulouse, France

⁴ Argelander-Institut für Astronomie (AIfA), Universität Bonn, Auf dem Hügel 71, 53121 Bonn, Germany

⁵ Universitäts-Sternwarte, LMU Munich, Scheinerstr. 1, 81679 München, Germany

⁶ Arnold Sommerfeld Center for Theoretical Physics, LMU Munich, Theresienstr. 37, 80333 München, Germany

⁷ Department of Astronomy, University of Geneva, Ch. d'Ecogia 16, CH-1290 Versoix, Switzerland

⁸ Department of Physics, National Cheng Kung University, 70101 Tainan, Taiwan

⁹ Department of Physical Science, Hiroshima University, 1-3-1 Kagamiyama, Higashi-Hiroshima, Hiroshima 739-8526, Japan

¹⁰ McWilliams Center for Cosmology, Department of Physics, Carnegie Mellon University, Pittsburgh, PA 15213, USA

¹¹ Subaru Telescope, National Astronomical Observatory of Japan, 650 N Aohoku Place Hilo HI 96720 USA

¹² Kobayashi-Maskawa Institute for the Origin of Particles and the Universe (KMI), Nagoya University, Nagoya, 464-8602, Japan

¹³ Institute for Advanced Research, Nagoya University, Nagoya 464-8601, Japan

¹⁴ Kavli Institute for the Physics and Mathematics of the Universe (WPI), The University of Tokyo Institutes for Advanced Study (UTIAS), The University of Tokyo, Chiba 277-8583, Japan

February 14, 2024

ABSTRACT

The evolution of the cluster mass function traces the growth of the linear density perturbations and can be utilized for constraining the parameters of cosmological and alternative gravity models. In this context, we present new constraints on potential deviations from general relativity by investigating the Hu-Sawicki parametrization of the $f(R)$ gravity with the first SRG/eROSITA All-Sky Survey (eRASS1) cluster catalog in the Western Galactic Hemisphere in combination with the overlapping Dark Energy Survey Year-3, KiloDegree Survey and Hyper Supreme Camera data for weak lensing mass calibration. For the first time, we present constraints obtained from cluster abundances only. When we consider massless neutrinos, we find a strict upper limit of $\log |f_{R0}| < -4.31$ at 95% confidence level. Massive neutrinos suppress structure growth at small scales, and thus have the opposite effect of $f(R)$ gravity. We consequently investigate the joint fit of the mass of the neutrinos with the modified gravity parameter. We obtain $\log |f_{R0}| < -4.12$ jointly with $\sum m_\nu < 0.44$ eV at 95% confidence level, tighter than the limits in the literature utilizing cluster counts only. At $\log |f_{R0}| = -6$, the number of clusters is not significantly changed by the theory. Consequently, we do not find any statistical deviation from general relativity from the study of eRASS1 cluster abundance. Deeper surveys with eROSITA, increasing the number of detected clusters, will further improve constraints on $\log |f_{R0}|$ and investigate alternative gravity theories.

Key words. modified gravity – cosmological parameters – galaxies: clusters: general – large scale structures of the universe

1. Introduction

Our understanding of the Universe has been altered significantly with the discovery of its accelerated expansion, first demonstrated by supernovae observations (Riess et al. 1998; Perlmutter et al. 1999). The paradigm of the standard cosmological model widely represents this unknown dark energy with a constant added in Einstein's gravitational equations Λ , the so-called cosmological constant. Other ingredients necessary to describe our cosmological model include a non-relativistic (*cold*) dark matter component that represents most of the mass fraction of the large-scale structures (LSS). These two components constitute the major fraction of the energy content of the present-day Universe and form the backbone of the concordance Λ CDM model. So far, when considered together with inflation, this parametrization is

relatively successful at describing the main observed properties of the universe (Planck Collaboration et al. 2020).

Galaxy clusters represent the most massive virialized structures in the Universe. The number density of clusters of galaxies per unit mass and redshift, i.e., cluster mass function, and their spatial distribution, i.e., the two-point correlation function and higher order statistics, have great potential to constrain the nature of dark energy and test the robustness of the underlying cosmological models (see Clerc & Finoguenov 2023, for a recent review). Cluster counts are currently the most efficient at placing constraints on the matter density parameter (Ω_m), the root mean square of the density fluctuations in spheres of 8 Mpc h^{-1} (σ_8), and the sum of the masses of the neutrinos ($\sum m_\nu$). Additionally, it also breaks the degeneracies between the cosmological parameters of other probes, such as the baryon acoustic oscillations

(BAO; Eisenstein et al. 2005; Alam et al. 2017), redshift space distortions (RSD; Percival & White 2009), the weak-lensing cosmic shear (Troxel et al. 2018; Asgari et al. 2021; Amon et al. 2022; Li et al. 2023), Supernovae type Ia (SNe Ia) and other distance ladders (Riess et al. 2019; Freedman et al. 2019), and the cosmic microwave background (CMB; Bennett et al. 2013; Planck Collaboration et al. 2020). Previous and ongoing cluster surveys across a wide wavelength range demonstrate the potential of cluster number counts as a powerful cosmological probe when the biases related to mass calibration are reduced through the utilization of the weak gravitational lensing observations (Mantz et al. 2015; Bocquet et al. 2019; Zubeldia & Challinor 2019; Ider Chitham et al. 2020; Garrel et al. 2022; Lesci et al. 2022; Sunayama et al. 2023; Fumagalli et al. 2023; Bocquet et al. 2023, 2024, among others). Modern cluster surveys, such as the eROSITA All-Sky cluster survey (see Bulbul et al. A&A subm.; Ghiradini et al. A&A subm.), are revolutionizing the field of cosmology, promising to reach the precision of the CMB experiments on cosmological parameters and have the potential to measure departures from Einstein’s theory of general relativity (GR) and test theories of dark energy (Wolf & Ferreira 2023). In addition to cluster abundance, eROSITA is probing cosmology through the spatial distribution of galaxy clusters (Seppi et al. A&A subm.), and the X-ray power spectrum (Garrel et al. in prep.). It also provides an avenue for testing alternative gravity theories, which could, in return, explain the late-time accelerated expansion of the Universe. Indeed, a way of explaining the Universe’s accelerated expansion is to modify the theory of gravitation on large scales while retaining GR in the high-density solar system and galactic scales. Potential departures from GR can be modeled by a set of theories in which the Ricci scalar (R), the quantity describing the infinitesimal volumes in curved space-time, is replaced in the Einstein-Hilbert action (Equation 1) by a generic function $f(R)$. One of the models introducing a physically motivated function is the one proposed by Hu & Sawicki (2007) (HS- $f(R)$ hereafter). This model has direct phenomenological implications. For example, Tsujikawa et al. (2009) and Gannouji et al. (2009) showed that it would significantly increase the structure formation rate, and thus, its predictions can be verified. In the context of cluster abundance studies, it increases the expected number density of massive dark matter halos (see figure 2). In order to observationally constrain this model, many efforts have been made in recent years to provide tools computing summary statistics measuring departures from GR. First, numerous codes adapt the standard Boltzmann solvers, e.g., CAMB (Lewis & Challinor 2011) and CLASS (Lesgourgues 2011) for modified gravity (MG hereafter) studies with alternative software such as EFTCAMB (Hu et al. 2014), hi_class (Zumalacárregui et al. 2017), MGCAMB (Zucca et al. 2019; Wang et al. 2023), or FRCAMB Xu (2015). These extensions can compute the power spectrum in different MG scenarios.

However, the hierarchical scenario of structure formation assumes that galaxy clusters originate from the gravitational collapse of matter overdensities. The cluster abundance can thus be obtained by computing the characteristics of this collapse in the corresponding theory (Kopp et al. 2013; Lombriser et al. 2013) while considering the standard power spectrum. Starting from this fact, several studies attempt to constrain the $f(R)$ parameters using clusters in the literature. As the first of the studies, Schmidt et al. (2009) uses a sample of 49 low redshift clusters detected by ROSAT and re-observed by Chandra (Vikhlinin et al. 2009) to constrain the HS- $f(R)$ model. This approach is combined with other cosmological probes by Lombriser et al. (2012), showing that the best constraints are obtained when cluster abundance is

considered. Cataneo et al. (2015) reported a robust upper limit for the value of the background scalar field $\log|f_{\text{R0}}| < -4.79$ by utilizing a sample of 224 ROSAT-detected clusters combined with CMB data. Additionally, Lombriser et al. (2013) and later Cataneo et al. (2016) developed a halo mass function (HMF) formalism for predicting accurate cluster abundances, which was followed by von Braun-Bates et al. (2017) and Gupta et al. (2022) formalisms. These studies explore the implication of $f(R)$ gravity in the halo formation process. In parallel, Hagstotz et al. (2019) developed an alternative method where the HMF modeling accounts for the massive neutrinos and modified gravity effects. The modifications of gravity are then encapsulated in the collapse model and the halo mass function parametrization. In this work, we use this approach to predict the cluster counts. We emphasize again that all the cosmological quantities related to the matter power spectrum are computed with the standard version of CAMB, without any need for an application of the modified Boltzmann solver. With 5259 clusters of galaxies selected in its cosmology sample in a wide redshift range $0.1 < z < 0.8$, the Western Galactic Half of the first eROSITA All-Sky Survey (eRASS1) has the statistical power to reach far beyond constraints available from any cluster survey in the literature. Consequently, this work utilizes the largest intracluster medium (ICM) selected cluster sample to date, in combination with weak lensing follow-up measurements for cluster masses and an accurate selection function to constrain deviations from GR by placing robust limits on the HS parametrization of $f(R)$ gravity.

The paper is organized as follows: in section 2, we describe the datasets used. Section 3 introduces the framework used to describe departures from GR in the HS- $f(R)$ gravity. Section 4 provides a detailed description of the statistical methods. Finally, section 5 presents the constraints on the HS- $f(R)$ gravity and comparison with the Λ CDM concordance model. Throughout this paper, we use the notation $\log \equiv \log_{10}$, and $\ln \equiv \log_e$.

2. Survey Data

The data used in this work is identical to the survey data presented in (Bulbul et al. A&A subm.; Kluge et al. A&A subm.; Ghiradini et al. A&A subm.; Grandis et al. A&A subm.; Kleinbreil 2023). We summarize the multi-wavelength data, including X-ray, optical, and weak lensing observations, utilized in this work in the following section.

2.1. eROSITA All-Sky Survey

The soft X-ray telescope, eROSITA, on board the Spectrum Roentgen Gamma Mission, completed its All-Sky Survey program on June 11, 2020, 184 days after the start of the survey. In this work, we use the data of the Western Galactic half of the eROSITA All-Sky survey ($359.9442 \text{ deg} > l > 179.9442 \text{ deg}$) belonging to the German eROSITA consortium. Bulbul et al. (A&A subm.); Kluge et al. (A&A subm.) compiled two catalogs of clusters detected in this region: primary galaxy groups and clusters catalog and the cosmology sample based on the catalog of the X-ray sources in the soft band (0.2–2.3 keV) provided in Merloni et al. (2024). We utilize the eRASS1 cosmology sample in this work, which is compiled adopting a selection cut of extent likelihood, $\mathcal{L}_{\text{ext}} > 6$ (see Bulbul et al. A&A subm., for further details). The optical identification of the clusters selected in the LS DR10-South common footprint produces a final cosmology sample of 5259 clusters of galaxies reaching purity levels of 95%, an ideal sample for the modified gravity studies. Unlike the

primary cluster catalog, the redshifts in the cosmology subsample are purely photometric measurements, allowing a consistent assessment of the systematics in our analysis. The total survey area covers a 12791 deg^2 region in the Western Galactic Hemisphere. The cont-rates are extracted with the 2D-image fitting tool MBProj2D as described in Bulbul et al. (A&A subm.) and are employed as a mass proxy in the weak lensing mass calibration likelihood (Ghiradini et al. A&A subm.).

2.2. Weak Lensing Survey Data

To perform our mass calibration in a minimally biased way, we utilize the deep and wide-area optical surveys for lensing measurements with the overlapping footprint with eROSITA in the Western Galactic Hemisphere. The three wide-area surveys used in this work for mass calibration include the Dark Energy Survey (DES), Kilo Degree Survey (KiDS), and the Hyper SupremeCam Survey (HSC). We briefly describe the weak lensing survey data here.

The three-year weak-lensing data (S19A) covered by the HSC Subaru Strategic Program (Aihara et al. 2018; Li et al. 2022) weak lensing measurements are made around the location of eRASS1 clusters using in the g , r , i , z , and Y bands in the optical. The total area coverage of HSC is $\approx 500 \text{ deg}^2$. The shear profile $g_r(\theta)$, the lensing covariance matrix that serves the measurement uncertainty, and the photometric redshift distribution of the selected source sample are obtained as the HSC weak-lensing data products for 96 eRASS1 clusters, with a total signal-to-noise of 40.

We utilize data from the first three years of observations of the Dark Energy Survey (DES Y3). The DES Y3 shape catalog (Gatti et al. 2021) is built from the r , i , z -bands using the METACALIBRATION pipeline (Huff & Mandelbaum 2017; Sheldon & Huff 2017). Considering the overlap between the DES Y3 footprint and the eRASS1 footprint, we produce tangential shear data for 2201 eRASS1 galaxy clusters, with a total signal-to-noise of 65 in the tangential shear profile. The details of the analysis and shear profile extraction are presented in Grandis et al. (A&A subm.).

We use the gold sample of weak lensing and photometric redshift measurements from the fourth data release of the Kilo-Degree Survey (Kuijken et al. 2019; Wright et al. 2020; Hildebrandt et al. 2021; Giblin et al. 2021), hereafter referred to as KiDS-1000. We extract individual reduced tangential shear profiles for a total of 236 eRASS1 galaxy clusters in both the KiDS-North field (101 clusters) and the KiDS-South field (136 clusters), as both have overlap with the eRASS1 footprint with a total signal-to-noise of 19.

The weak lensing data in the mass calibration process is described in detail and published in (Ghiradini et al. A&A subm.; Grandis et al. A&A subm.; Kleinebreil 2023). We do not process the data but adopt the framework from (Ghiradini et al. A&A subm.).

3. Modified Gravity Framework

The evolution of the large-scale structures of the Universe is sensitive to modification to the standard frameworks of GR and Λ CDM. To investigate potential discrepancies, we need to probe different scales and epochs. Figure 1 shows the redshift and scale sensitivity of the most common cosmological probes. Galaxy cluster number counts efficiently place constraints on the low redshift/large-scale regime not explored by other probes. In

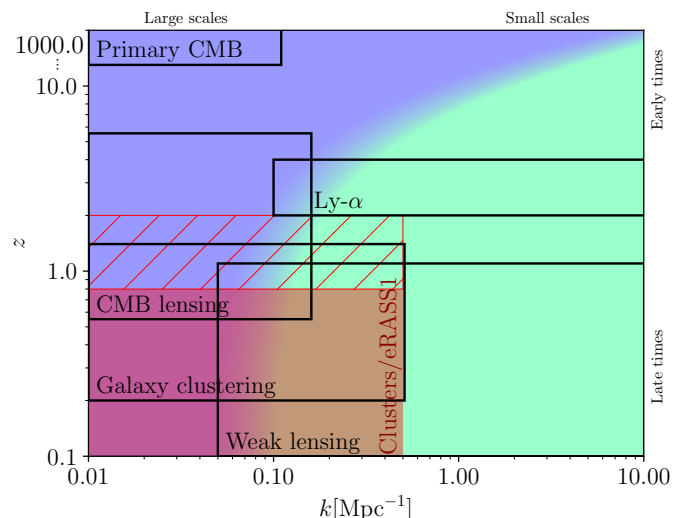


Fig. 1: The estimation of the scale and redshift sensitivity of the different cosmological probes, adapted from Preston et al. (2023). The background colors, from blue to green, represent the transition from the linear to the non-linear regime. We represent cluster abundance with the red rectangle. The cosmology sample of eRASS1 spans the redshift range $0.1 < z < 0.8$, as represented by the solid red rectangle. Future data releases and experiments will increase the upper limit of this interval to the hatched red rectangle. Cluster abundance experiments thus probe a specific regime at large spatial scales and nearby Universe, offering a complementary window on structure formation. The experiments with cluster clustering (Seppi et al. A&A subm.) and X-ray power spectrum (Garrel et al. in prep.) are omitted here. In particular, the X-ray power spectrum might probe smaller scales.

this section, we describe the framework explored in this paper, namely the HS- $f(R)$ model.

3.1. HS- $f(R)$ gravity in the context of cluster counts

We choose to test the modified gravity model that consists of a modification of the Einstein-Hilbert action in the following form:

$$S = \int dx^4 \sqrt{-g} \left(\frac{R + f(R)}{16\pi G} + \mathcal{L}_m \right), \quad (1)$$

where \mathcal{L}_m represents the Lagrangian of the matter field, R is the Ricci scalar and $f(R)$ represents the extension to GR, for which $f(R) = -2\Lambda$. In the context of $f(R)$ gravity, many functional forms are proposed (see De Felice & Tsujikawa 2010, for a review). Throughout this paper, we focus on the Hu & Sawicki (2007) model, which formalizes $f(R)$ as

$$f(R) = -2\Lambda \frac{R^n}{R^n + m^{2n}}, \quad (2)$$

where m^2 represents the curvature scale, and Λ and n (the scaling index) are constants. We point out that the model does not include a cosmological constant as $f(R) \rightarrow 0$ when $R \rightarrow 0$. In the high curvature regime ($R \gg m^2$), equation (2) becomes

$$f(R) = -2\Lambda \frac{R^n}{R^n + m^{2n}} = -2\Lambda \frac{1}{1 + \left(\frac{m^2}{R}\right)^n} \sim -2\Lambda \left(1 - \left(\frac{m^2}{R}\right)^n \right).$$

To express this function in terms of $f_{\text{R}}(R) = df/dR$. Then, $f(R)$ becomes

$$f(R) = -2\Lambda - \frac{f_{\text{R}0} \bar{R}_0^{-n+1}}{n R^n},$$

where we have defined value of the field $f_{\text{R}0} = df/dR(R_0) = -2n\Lambda m^{2n}/\bar{R}_0^{n+1}$ at $z=0$, \bar{R}_0 is the Ricci scalar at $z = 0$ and overbars denote background quantities. State-of-the-art numerical simulations are required to build a precise HMF suitable for cluster abundance cosmology. In these simulations, it is common to use $n = 1$ (e.g. [Oyaizu 2008](#); [Zhao et al. 2011](#); [Giocoli et al. 2018](#)). For consistency with the HMF calibration method, we thus freeze the scaling index to unity. We finally obtain

$$f(R) \approx -2\Lambda - f_{\text{R}0} \frac{\bar{R}_0^2}{R}. \quad (3)$$

In this model, we note that when $|f_{\text{R}0}| \rightarrow 0$, we recover the usual GR action with a cosmological constant in equation (1). Thus, we interpret Λ as the cosmological constant. The only parameter quantifying the deviations from GR is $f_{\text{R}0}$. When $|f_{\text{R}0}| \ll 1$, the background expansion is not distinguishable from GR. In this paper, our main goal is to measure $f_{\text{R}0}$ or to set an upper limit on its value. In the rest of this section, we briefly describe the behavior of this model.

The variational principle applied on the action in Equation (1) leads to the modified Einstein's equation:

$$G_{\mu\nu} - f_{\text{R}} R_{\mu\nu} - \left(\frac{f}{2} - \square f_{\text{R}} \right) g_{\mu\nu} - \nabla_{\mu} \nabla_{\nu} f_{\text{R}} = 8\pi G T_{\mu\nu}. \quad (4)$$

As usual, the equation (4) provides the equation of motion of the scalar field f_{R} :

$$\nabla^2 \delta f_{\text{R}} = \frac{a^2}{3} (\delta R(f_{\text{R}}) - 8\pi G \delta \rho_m), \quad (5)$$

where δ denotes small perturbations of the related quantities. This also provides a Poisson-like equation given by

$$\nabla^2 \psi = \frac{16\pi G}{3} a^2 \rho_m - \frac{a^2}{6} \delta R(f_{\text{R}}). \quad (6)$$

For a better understanding of the behavior in this model, we provide the thin-shell condition example first introduced by [Khoury & Weltman \(2004\)](#) and adapted in [Li et al. \(2012\)](#) and [Lombriser et al. \(2013\)](#). Since GR is well constrained in high-density environments like the solar system, we want to recover it at small scales: this is the so-called *screening mechanism*. As an illustration, let us consider a top-hat overdensity of radius R_{in} . Then, the gravitational pull exerted on a particle of mass m outside of the overdensity can be expressed as

$$F = G \frac{M_{\text{in}} m}{r^2} \left(1 + \frac{1}{3} \frac{\Delta R}{R_{\text{in}}} \right), \quad (7)$$

where M_{in} is the mass inside the top hat overdensity, r is the distance to the center and $\Delta R/R_{\text{in}}$ is the screening factor defined as

$$\frac{\Delta R}{R_{\text{in}}} = \min \left\{ \frac{3|f_{\text{R}}^{\text{in}} - f_{\text{R}}^{\text{out}}|}{2\phi_{\text{N}}}, 1 \right\}, \quad (8)$$

where ϕ_{N} is the Newtonian gravitational potential $\phi_{\text{N}} = GM_{\text{in}}/R_{\text{in}}$, f_{R}^{in} and $f_{\text{R}}^{\text{out}}$ are the values of the scalar field inside

and outside of the top-hat overdensity. Considering that the background expansion is considered in Λ CDM, we can approximate the background Ricci scalar to the one expected in this model. Inside the top hat overdensity, we consider that the screening mechanism is active, i.e., we recover GR. We can then express the scalar field as

$$f_{\text{R}}^{\text{in}} = f_{\text{R}0} \left(\frac{1 + 4\Omega_{\Lambda 0}/\Omega_{\text{m}0}}{\rho_{\text{m}}^{\text{in}}/\rho_{\text{m}0} + 4\Omega_{\Lambda 0}/\Omega_{\text{m}0}} \right), \quad (9)$$

where $\rho_{\text{m}}^{\text{in}}$ is the density inside the considered region. In equation 9, we note that the scalar field values become smaller in high-density regions ($\rho_{\text{m}0} \ll \rho_{\text{m}}^{\text{in}}$). Thus in Equation 8, the screening factor, becomes

$$\frac{\Delta R}{R_{\text{in}}} \sim \frac{3|f_{\text{R}}^{\text{out}}|}{2\phi_{\text{N}}}.$$

The condition for the screening to be activated is $\Delta R/R_{\text{in}} \ll 1$. Thus we must have that $|f_{\text{R}}^{\text{out}}| \ll \phi_{\text{N}}$. Since f_{R} is a monotonic function of time, a relevant condition would be to have

$$|f_{\text{R}0}| < \phi_{\text{N}}.$$

For massive galaxy clusters, the Newtonian potential (in natural units) is of order 10^{-5} . Thus, for these gravitationally bound systems, the deviation to GR is screened (i.e., suppressed) when $|f_{\text{R}0}| < 10^{-5}$ (see section 3.3). Overall, the HS- $f(R)$ gravity model is defined with only one additional parameter: $f_{\text{R}0}$. This formalism allows the recovery of GR in the regimes necessary from observational constraints. In the next section, we describe the formalism predicting the dark matter halo abundance.

3.2. The $f(R)$ halo mass function

The density of clusters per unit mass and redshift is modeled as follow:

$$\frac{dn}{d \ln M} = \frac{\rho_{\text{m},0}}{M} \frac{d \ln \sigma^{-1}}{d \ln M} f(\sigma), \quad (10)$$

where $\rho_{\text{m},0}$ is the matter density at present, $f(\sigma)$ is the multiplicity function, and $\sigma(R, z)$ is defined by

$$\sigma^2(R, z) = \frac{1}{2\pi^2} \int_0^{\infty} k^2 P(k, z) \left(\frac{3j_1(kR)}{kR} \right)^2 dk, \quad (11)$$

where $j_1(x) = (\sin(x) - x \cos(x))/x^2$ is the spherical Bessel function of the first kind of order one, and $P(k)$ is the matter power spectrum. We follow the approach developed in [Hagstotz et al. \(2019\)](#) to describe the specific behavior of the HMF in the HS- $f(R)$ framework when compared to the standard fitting functions and emulators ([Tinker et al. 2008](#); [Despali et al. 2016](#); [Bocquet et al. 2020](#); [Euclid Collaboration et al. 2023a](#)) obtained from simulations assuming standard GR. The main advantage of this formalism is that the entire framework is derived from the collapse of the structures in $f(R)$ gravity, with standard computations for the power spectrum. Deviations from the GR HMF are modeled as follows: the multiplicity function can be written as in Equation (10). The goal is to correct the multiplicity function by a factor encapsulating the deviations from GR; therefore,

$$f^{f(R)}(\sigma) = f^{\text{GR}}(\sigma) \cdot \eta(f_{\text{R}0}, \sigma), \quad (12)$$

where the correcting factor is given by

$$\eta(f_{R0}, \sigma) = \frac{f_k^{f(R)}(f_{R0}, \sigma)}{f_k^{\text{GR}}(\sigma)}. \quad (13)$$

The the multiplicity functions including the subscript k in the correcting factor are defined as follow. In the formalism of the multiplicity function, the density field δ realizes a random walk (i.e., a Markov process) when smoothed by a simple top-hat filter in k -space, with the radius R defined in Equation (11). This means that in the trajectories $\delta(R)$, the next positions depend only on the current position. The multiplicity functions in Equation (13) are obtained that way and are noted with the subscript k . They are not realistic enough to describe the halo abundance. The $f(R)$ properties are encoded on the collapse of structures and not on the statistics of the density field, and their ratio is well suited to quantify departure from GR. However, more realistic filters should be considered to derive a proper fitting function, which causes departures from the uncorrelated random walk. Any multiplicity function, including these non-Markovian corrections found in the literature, can be applied for f^{GR} . In this work, we use the [Tinker et al. \(2008\)](#) as $f^{\text{GR}}(\sigma)$. We emphasize that the resulting fitting function for HMF we use in this work was initially calibrated for masses defined as M_{200m} . We convert the HMF to M_{500c} as eRASS1 mass measurements are calibrated for M_{500c} . Additionally, doing so allows us to stay consistent with the standard Λ CDM cosmology analysis presented in [Ghirardini et al. \(A&A subm.\)](#). In the case of GR, the multiplicity function is given by

$$f_k^{\text{GR}}(\sigma) = \sqrt{\frac{2a}{\pi}} \frac{\delta_c}{\sigma} \exp\left(-a \frac{(\delta_c + \beta\sigma^2)^2}{2\sigma^2}\right), \quad (14)$$

, where a and β are fixed to the values provided in [Hagstotz et al. \(2019\)](#), and δ_c is the critical density for the collapse in GR given by the appendix C of [Nakamura & Suto \(1997\)](#)

$$\delta_c^{\text{GR}}(z) = \frac{3(12\pi)^{2/3}}{20} \left(1 - 0.012299 \log\left(1 + \frac{\Omega_m^{-1} - 1}{(1+z)^3}\right)\right). \quad (15)$$

The multiplicity function in the case of HS- $f(R)$ gravity for non-markovian correction follows:

$$f_k^{f(R)}(\sigma) = \sqrt{\frac{2a}{\pi}} \frac{1}{\sigma} e^{-a\bar{B}^2/(2\sigma^2)} \left(\delta_c^{f(R)} - \frac{3M}{2} \frac{\partial \delta_c^{f(R)}}{\partial M} \frac{\partial \ln \sigma}{\partial \ln R} \right), \quad (16)$$

where a is a constant. \bar{B} is the barrier, the threshold beyond which collapse structures are formed. This threshold follows

$$\bar{B} = \delta_c^{f(R)}(f_{R0}, M, z) + \beta\sigma^2,$$

with β being another constant. The key of this formalism is thus to compute the spherical collapse threshold in $f(R)$ gravity. For a review, we point the reader to [Kopp et al. \(2013\)](#) and the previous references of this section. Here, we provide the numerical solutions used for the collapse model:

$$\delta_c^{f(R)}(f_{R0}, M, z) = \delta_c^{\text{GR}}(z) \times \Delta(f_{R0}, M, z) \quad (17)$$

where the $\Delta(f_{R0}, M, z)$ is given by:

$$\Delta(f_{R0}, M, z) = 1 + b_2 (1+z)^{-a_3} \left(m_b - \sqrt{m_b^2 + 1} \right) + b_3 \left(\tanh(m_b) - 1 \right). \quad (18)$$

The different parameters of the collapse model are defined as follows, as they were originally fitted:

$$\begin{cases} b_2 & = 0.0166 \\ a_3(f_{R0}) & = 1 + \exp\left(-2.08 (\log |f_{R0}| + 5.56)^2\right) \\ m_b(f_{R0}, M, z) & = (1+z)^{a_3} (\log M - m_1(1+z)^{-a_4}) \\ & \quad m_1(f_{R0}) = \mu_1 \log |f_{R0}| + \mu_2 \\ & \quad a_4(f_{R0}) = \alpha_4 \left(\tanh(0.69 (\log |f_{R0}| + 6.65)) + 1 \right) \\ b_3(f_{R0}) & = \beta_3 (2.41 - \log |f_{R0}|) \end{cases} \quad (19)$$

Three values are then required to describe the collapse threshold in the HS- $f(R)$ parametrization. Those are represented by the parameters μ_1, μ_2, α_4 and β_3 . In this work, we use the best-fit value given by [Hagstotz et al. \(2019\)](#).

One can verify that this parametrization converges to the standard GR threshold for collapse $\delta_c^{\text{GR}}(z)$ (15), when $|f_{R0}|$ takes small values.

The HMF derived here is computed for M_{200m} , while the eRASS1 cosmology pipeline considers M_{500c} . Thus, we follow [Hu & Kravtsov 2003](#) to convert the mass: we first compute the HMF from [Tinker et al. \(2008\)](#) $dn/d \ln M_{500c}$ for a broad range of halo mass M_{500c} and convert these masses assuming the mass concentration relation from [Duffy et al. \(2008\)](#) and the Navarro, Frenk, and White (NFW) density profile ([Navarro et al. 1996](#)). The resultant $f(R)$ HMF thus follows

$$\frac{dn^{f(R)}}{d \ln M_{500c}} = \frac{\rho_{m,0}}{M_{500c}} \left| \frac{d \ln \sigma}{d \ln M_{500c}} \right| f_{\text{Tinker2008}}(\sigma(M_{500c})) \times \frac{f_k^{f(R)}(\sigma(M_{200m}(M_{500c})))}{f_k^{\text{GR}}(\sigma(M_{200m}(M_{500c})))}. \quad (20)$$

This equation represents the HMF used in this work, although we note that the uncertainties related to the HMF can impact our constraints ([Salvati et al. 2020; Artis et al. 2021](#)). Figure 2 shows the evolution of the HMF when $\log f_{R0}$ increases. Due to different numerical simulations, halo finders, various fitting functions used in previous work, and baryonic effects, we expect the departure between the standard GR HMFs in the literature to be as high as 10% ([Knebe et al. 2013; Euclid Collaboration et al. 2023a](#)). Additionally, the model used in this work presents up to 20% differences with the predictions of [Cataneo et al. \(2016\)](#). These systematic uncertainties are accounted for following [Costanzi et al. \(2019\)](#) i.e. we compute the HMF as

$$\frac{d\tilde{n}^{f(R)}}{d \ln M_{500c}} = \frac{dn^{f(R)}}{d \ln M_{500c}} (s \ln(M/10^{14} M_\odot) + q), \quad (21)$$

where q and s represent the errors respectively on the amplitude and slope of the HMF. Adopting a conservative approach, we use priors $q \sim \mathcal{N}(1, 0.5)$ and $s \sim \mathcal{N}(0, 0.5)$.

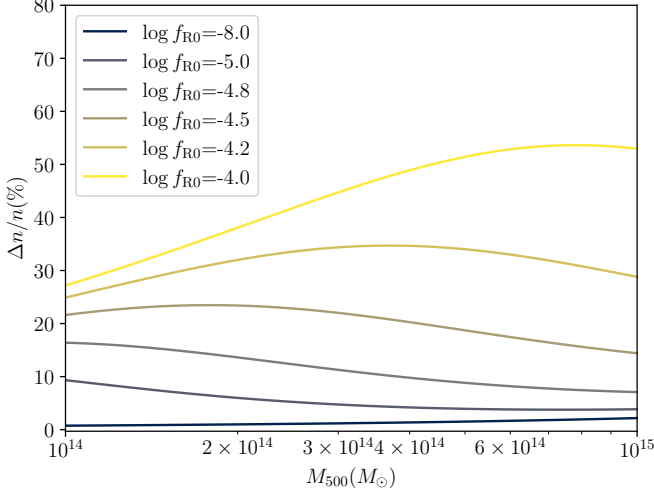


Fig. 2: Relative difference (in percentage) of the HMF when f_{R0} increases. We note that $\Delta n = dn/d \ln M(f_{R0}) - dn/d \ln M$, where $dn/d \ln M(f_{R0})$ is the HMF described with equation 20 and $dn/d \ln M$ is obtained with the GR fitting function from Tinker et al. (2008). Increased values of f_{R0} create more massive halos.

3.3. Weak lensing mass calibration in modified gravity

In this work, we aim to constrain modifications of the theory of gravity with the cluster halo mass function calibrated with the scaling relation between the X-ray count rate and the weak lensing shear data. Therefore, the predictions for the weak lensing signal of galaxy clusters in the modified gravity theories are needed for self-consistent analysis. As discussed in the following, we use the prediction from GR for the WL signal of massive clusters by simply utilizing the calibration performed by Grandis et al. (A&A subm.). For readability, we provide the basis of the analysis and critical aspects (see Bartelmann & Schneider 2001, for detailed description and review). In the framework of GR, the gravitational potential of a lens cluster deflects the light from distant background sources. The surface brightness S_s at position θ of a source with negligible dimensions compared to the lens size is as follows:

$$S_{\text{obs}}(\theta) = S_s(\mathbf{A}\theta), \quad (22)$$

where \mathbf{A} is the lensing distortion matrix. It is written as

$$\mathbf{A} = \begin{pmatrix} 1 - \kappa - \gamma_1 & \gamma_2 \\ \gamma_2 & 1 - \kappa + \gamma_1 \end{pmatrix}. \quad (23)$$

The convergence κ relates to isotropic transformations of the image, while the shear components (γ_1, γ_2) are linked to the image distortion. The main transformations of the image are described by these two quantities, and they are computed as follow: the total distribution of mass in clusters is assumed to follow the NFW profile introduced in Navarro et al. (1996), which is well fit- simulated DM, and defined as:

$$\rho(r) = \frac{\delta(c_\Delta)\rho_c(z)}{\frac{r}{r_\Delta/c_\Delta} \left(1 + \frac{r}{r_\Delta/c_\Delta}\right)^2}, \quad (24)$$

where r_Δ is the radius defined such that the mean density of the enclosed volume is Δ times the mean density of the universe.

$\rho_c = 3H^2/8\pi G$ is the critical density and c_Δ is the concentration parameter. δ is a function that results from the definition of the radius r_Δ and reads:

$$\delta(c_\Delta) = \frac{\Delta}{3} \frac{c_\Delta^3}{\ln(1 + c_\Delta) - c_\Delta(1 + c_\Delta)}. \quad (25)$$

This mass profile creates a gravitational potential noted ϕ . We will note the lens cluster l and background sources (typically galaxies). In the thin lens approximation (the typical size of the lens is negligible compared to the distance), we can write the lensing potential of a cluster as

$$\psi(\theta) = \frac{2}{c^2} \frac{D_{ls}}{D_l D_s} \int \phi(D_l \theta, z) dz, \quad (26)$$

where $\theta = (\theta_1, \theta_2)$ is the position on the sky. D_{ls} , D_l , and D_s are respectively the distance between the lens cluster and the source galaxy, the distance between the lens and the observer and the galaxy. The convergence and shear component can be expressed as a function of the derivatives of the lensing potential through

$$\begin{cases} \kappa(\theta) = \frac{1}{2} \left(\frac{\partial^2 \psi}{\partial \theta_1^2} + \frac{\partial^2 \psi}{\partial \theta_2^2} \right) \\ \gamma_1(\theta) = \frac{1}{2} \left(\frac{\partial^2 \psi}{\partial \theta_1^2} - \frac{\partial^2 \psi}{\partial \theta_2^2} \right) \\ \gamma_2(\theta) = \frac{\partial^2 \psi}{\partial \theta_1 \partial \theta_2} \end{cases}. \quad (27)$$

These expressions, combined with the definition of the lensing potential (26), lead to the following: if we define the surface mass density as

$$\Sigma(R) = 2 \int_0^\infty \rho(R, z) dz, \quad (28)$$

where the matter density follows the NFW profile (24), the convergence profile is expressed as

$$\kappa(R) = \frac{\Sigma(R)}{\Sigma_c}, \quad (29)$$

and the radial dependence of the tangential shear follows

$$\gamma_t(R) = \frac{\Sigma(< R) - \Sigma(R)}{\Sigma_c}, \quad (30)$$

where $\Sigma(< R)$ is the mean surface mass density in the radius R , and the $\Sigma_c = c^2/4\pi G \cdot D_s/D_l D_{ls}$. These quantities are derived in Wright & Brainerd (2000). The weak lensing mass calibration is performed through the *reduced tangential shear*

$$g_t(R) = \frac{\gamma_t(R)}{1 - \kappa(R)}. \quad (31)$$

The reduced tangential shear profiles are related to the underlying mass through $P(\hat{g}_t | M_{\text{WL}}, \hat{z})$ (see section 4.2). Since it is the consequence of the gravitational potential, it carries the necessary information on the underlying mass. To summarize, we assumed a standard lens equation resulting from GR to constrain our masses.

In this work, we consider one specific way of testing potential deviations: we probe the Hu-Sawicki parameterization of the $f(R)$ gravity.

The theory of gravity impacts cluster WL in two ways:

1. the paths of light through the cluster's gravitational potential might be altered by the modified theory, leading to the same lensing potential (Bekenstein & Sanders 1994) causing a different distortion in the shape of background galaxies and
2. the effective Newtonian potential of galaxy clusters in a modified theory might deviate from the one predicted in GR.

The first point is of no concern in the modification we explore. In the case of $f(R)$ gravity, the cosmic expansion remains the same (see section 3.1), but the geodesics are potentially affected. However, Schmidt (2010) showed that they remain virtually unchanged, up to a negligible factor of the order $\lesssim 10^{-4}$. We can thus use the generic lensing equations in HS- $f(R)$ gravity.

Halo matter profiles in $f(R)$ gravity have been extensively studied by Mitchell et al. (2018); Ruan et al. (2023), focusing on the mass concentration relation and the 3D density profiles. Neither of these two observables matches exactly the 2D projected matter density maps needed to anchor the WL mass calibration in a cluster cosmological context (Grandis et al. 2021a). Nonetheless, the general findings of Mitchell et al. (2018) about the maximal halo mass at which halos become fully screened can still be applied. That work finds that halos with a mass larger than $10^{p_2} h^{-1} M_\odot$ are screened and thus behave like in GR. The parameter is given by

$$p_2 = 1.50 (\log |f_{R0}| - \log(1 + z)) + 21.6, \quad (32)$$

where we round before the numerical errors reported in Mitchell et al. (2018). We shall evaluate this expression at $z = 0.1$, the lower redshift limit of our cluster sample. Given that we are working with an X-ray-selected sample, this is also the redshift at which we reach the lowest limiting mass. For the values $\log_{10} |f_{R0}| = 5.25, 5.5, 6$ we find $p_2 = 13.69, 13.31, 12.56$. The first value of p_2 correspond to a mass of $10^{13.85} M_\odot$. Considering that 95.4% of the objects in the cosmology sample have an estimated mass greater than this value, we can argue that the cluster one halo regime that we analyze is also unaltered in the $f(R)$ gravity parameter space we explore.

4. Statistical inference

This section provides a brief description of the cluster cosmology inference pipeline. A detailed review can be found in the Λ CDM eRASS1 cosmology results (Ghiradini et al. A&A *subm.*). The main element is that the cluster abundance statistic follows a Poisson statistic (i.e., cluster abundance as a function of their observable is a Poisson process), coupled with weak lensing shear measurements, calibrating the scaling relation between mass and X-ray observable. A mixture model for eliminating the contamination due to active galactic nuclei (AGN) and background fluctuations misclassified as clusters in the eRASS1 cosmology subsample is employed to perform a precision cosmology experiment.

We express λ as the intensity of the Poisson process (the number density of objects per unit of observable) and x as the vector of the observables. This intensity depends on the model, and we note Θ , the set of cosmological parameters. By definition, the expected number of objects whose observable properties belong to the sub-sample Ω of the observable parameter space follows;

$$N_{\{x \in \Omega\}}(\Theta) = \int_{\Omega} \lambda(x|\Theta) dx. \quad (33)$$

In our model, the global observable vector is defined as

$$x = \{\widehat{C}_R, \widehat{z}, \widehat{\lambda}, \mathcal{H}, g_+\},$$

where \widehat{C}_R are the observed count rate, \widehat{z} are the observed photometric redshifts, $\widehat{\lambda}$ is the observed richness, \mathcal{H} is the sky positions, which need to be considered due to the uneven exposure of the survey, and g_+ is the shear profile obtained from the different weak lensing surveys described in section 2.2. The intensity of the process thus described the number density of the objects in the parameter space. The Poisson realization of the expected value $N_{\{x \in \Omega\}}(\Theta)$. In the framework that we adopt in this paper, we need to describe the intensity for the different species that we are considering to predict the abundance of the objects. Then, the general shape of the Poisson log-likelihood will follow;

$$\ln \mathcal{L}(\Theta) = \sum_i \ln(\lambda(x_i|\Theta)) - \int_x \lambda(x|\Theta) dx, \quad (34)$$

where the index i runs over the observed objects. Using the Poisson likelihood, we neglect the cosmic variance (Hu & Kravtsov 2003) and the super sample variance (Lacasa & Grain 2019) as these effects are sub-dominant given the area covered by eRASS1 and the limited number of clusters included in this analysis (see Ghiradini et al. A&A *subm.*, for discussion). Our catalog contains three classes of objects: galaxy clusters (C), which are of interest, and contaminants, e.g., AGN, background fluctuations misclassified as clusters (NC). Our model simultaneously accounts for the cluster counts and the contaminant fractions through the Poisson mixture model. The total density is the sum of the three-component model;

$$\lambda_{\text{tot}}(x|\Theta) = \lambda_C(x|\Theta) + \lambda_{\text{AGN}}(x) + \lambda_{\text{NC}}(x). \quad (35)$$

In terms of the total number of objects in each class, we obtain

$$N_{\text{tot}}(\Theta) = N_C(\Theta) + f_{\text{AGN}} N_{\text{tot}}(\Theta) + f_{\text{NC}} N_{\text{tot}}(\Theta), \quad (36)$$

where f_{AGN} and f_{NC} are the respective fractions of contaminants. Consequently, we can express the number of AGN, false detections, and the total number of objects in the catalog as a function of the cosmology-dependent number of cluster N_C :

$$\begin{cases} N_{\text{tot}}(\Theta) = (1/(1 - f_{\text{AGN}} - f_{\text{NC}}))N_C(\Theta) \\ N_{\text{AGN}}(\Theta) = (f_{\text{AGN}}/(1 - f_{\text{AGN}} - f_{\text{NC}}))N_C(\Theta) \\ N_{\text{NC}}(\Theta) = (f_{\text{NC}}/(1 - f_{\text{AGN}} - f_{\text{NC}}))N_C(\Theta) \end{cases}. \quad (37)$$

Starting from the formalism above, we can write the total number of objects is written as

$$N_{\text{tot}}(\Theta) = \frac{1}{1 - f_{\text{AGN}} - f_{\text{NC}}} \int_x \lambda_C(x|\Theta) dx, \quad (38)$$

and that the number density of contaminants follows $\lambda_{\text{AGN}}(x|\theta) = N_{\text{AGN}}(\Theta)\mathcal{P}_{\text{AGN}}(x)$, and $\lambda_{\text{NC}}(x|\theta) = N_{\text{NC}}(\Theta)\mathcal{P}_{\text{NC}}(x)$. In this equation, \mathcal{P} describes the probability distribution function of the respective object, depending on the observables. These terms are described in 4.3. Finally, the likelihood 34 becomes

$$\ln \mathcal{L}(\Theta) = \sum_i \ln \left(\lambda_C(x_i|\Theta) + N_{\text{AGN}}(\Theta) \mathcal{P}_{\text{AGN}}(x_i) + N_{\text{NC}}(\Theta) \mathcal{P}_{\text{NC}}(x_i) \right) - \frac{1}{1 - f_{\text{AGN}} - f_{\text{NC}}} \int_x \lambda_C(x|\Theta) dx. \quad (39)$$

Separating the mass calibration likelihood from the number count likelihood is performed through the method described in the appendix of [Bocquet et al. \(2015\)](#). For the clusters belonging to the footprints of the WL surveys, the number density becomes

$$\lambda_C(x_{\setminus\{g_+\}}, g_+|\Theta) = \lambda_C(x_{\setminus\{g_+\}}|\Theta) \mathcal{P}(g_+|x_{\setminus\{g_+\}}, \Theta). \quad (40)$$

This formalism is applied in Equation 39 and allows for the calibration of X-ray and optical scaling relations. See section 4.2 and [Ghiradini et al. \(A&A subm.\)](#) for the details of the mass calibration.

In the following sections, we briefly describe the components of Equation 39. The cluster abundance term λ_C is described in 4.1, the weak lensing likelihood is given in section 4.2, and the mixture model accounting for contamination is provided in 4.3.

4.1. Cluster abundance likelihood

The term λ_C of Equation 39 represents the expected number density of clusters. It is obtained through

$$\lambda_C = \frac{dN_C}{d\hat{C}_R d\hat{z} d\hat{H}} = \int_z \int_M \int_{C_R} \mathcal{P}(I|C_R, z, \hat{H}) \mathcal{P}(\hat{C}_R|C_R) \mathcal{P}(C_R|M, z) \mathcal{P}(\hat{z}|z) \frac{dn}{dM} \frac{dV}{dz} dM dz dC_R. \quad (41)$$

dn/dM is the halo mass function, dV/dz is the comoving volume, and $\mathcal{P}(I|C_R, z, \hat{H})$ is the probability of detecting a cluster i.e. the selection function, the fraction of detected objects at a given observed sky position, redshift and count rates, given in [\(Clerc 2023\)](#). We note that the fraction of detected objects is estimated for a Λ CDM cosmology. We assume that this quantity is not significantly modified by the models considered in this work. The other terms are explained in the following. Consistently with [\(Ghiradini et al. A&A subm.\)](#), the count rates are assumed to be linked to the underlying mass of the objects through [\(Ghiradini et al. A&A subm.\)](#)

$$\left\langle \ln \frac{\overline{C_R}}{C_{R,p}} \middle| M, z \right\rangle = \ln A_X + b_X(M, z) \cdot \ln \frac{M}{M_p} + e_X(z), \quad (42)$$

where $C_{R,p} = 0.1$ cts/s and $M_p = 2 \times 10^{14} M_\odot$ are the pivot count rates and mass. All the masses are expressed in solar masses M_\odot . The other terms are

$$b_X(M, z) = \left(B_X + C_X \cdot \ln \frac{M}{M_p} + F_X \cdot \ln \frac{1+z}{1+z_p} \right), \quad (43)$$

where $z_p = 0.35$ is the pivot redshift, and

$$e_X(z) = D_X \cdot \ln \frac{d_L(z)}{d_L(z_p)} + E_X \cdot \ln \frac{E(z)}{E(z_p)} + G_X \cdot \ln \frac{1+z}{1+z_p}, \quad (44)$$

where d_L is the luminosity distance, $E(z) = H(z)/H_0$ is the evolution function. The parameters $\{A_X, B_X, C_X, D_X, E_X, F_X\}$ are fitted jointly with the cosmological parameters to provide consistency and avoid astrophysical biases. We assume that the true count rates are the following,

$$C_R \sim \text{Log-N}(\overline{C_R}(M, z), \sigma_X),$$

where Log-N characterizes the log-normal distribution, $\overline{C_R}(M, z)$, is the output of the scaling relation in Equation 42, and σ_X is the dispersion on the selection function, fitted together with the cosmological parameters. We also include the measurement errors on count rates fitted by the MultiBand Projector in 2D (MBProj2D) tool [\(Sanders et al. 2018\)](#), and the observed count rates are

$$\hat{C}_R \sim \text{Log-N}(C_R, \hat{\sigma}),$$

where $\hat{\sigma}$ is fixed at the value given by the X-ray processing pipeline, MBProj2D (see [Bulbul et al. A&A subm.](#), for details). The observed redshifts are obtained through eROMAPPer, the optical identification tool (see [Kluge et al. A&A subm.](#)) as in the following

$$P(\hat{z}|z) = (1 - c_z) \cdot \mathcal{N}(b_z \cdot z, \sigma_z(1+z)) + c_z \cdot \mathcal{N}(b_z \cdot z + c_{\text{shift},z}, \sigma_z(1+z)), \quad (45)$$

where c_z, b_z, σ_z and $c_{\text{shift},z}$ are the fitted parameters of the distribution. The richness, proxy for the number of galaxies belonging to a given cluster, is computed starting from [Grandis et al. \(2021b\)](#) as

$$\langle \ln \lambda|M, z \rangle = \ln A_\lambda + b_\lambda(z) \ln \left(\frac{M}{M_p} \right) + C_\lambda \ln \left(\frac{1+z}{1+z_p} \right), \quad (46)$$

where all the masses are expressed in solar mass (M_\odot), and the redshift dependence of the mass slope follows

$$b_\lambda(z) = B_\lambda + D_\lambda \ln \left(\frac{1+z}{1+z_p} \right). \quad (47)$$

The optical richness is not one of the main observables used in the mass calibration. It is only used to eliminate the contamination in the sample through the mixture method. We keep the richness limit low ($\hat{\lambda} > 3$) to ensure that no additional optical selection effects are introduced in the analysis.

4.2. Weak-lensing likelihood

An essential step between the cluster number counts and X-ray observables obtained from the eROSITA survey and the halo mass function is the calibration of the cluster mass scaling relations. We utilize the weak lensing shear measurements in calibrating cluster scaling relations as it is currently the most reliable method with minimal bias available [\(Euclid Collaboration et al. 2023b\)](#). We use the surveys, i.e., the Dark Energy Survey (DES), the Kilo Degree Survey (KiDS), and the HyperSupreme Cam (HSC), presented in section 2 to achieve this goal. Following [\(Grandis et al. A&A subm.\)](#) we assume a relation between weak lensing inferred masses and true mass in the following form;

$$\left\langle \ln \frac{M_{\text{WL}}}{M_p} \middle| M, z \right\rangle = b(z) + b_M \ln \left(\frac{M}{M_p} \right) \quad (48)$$

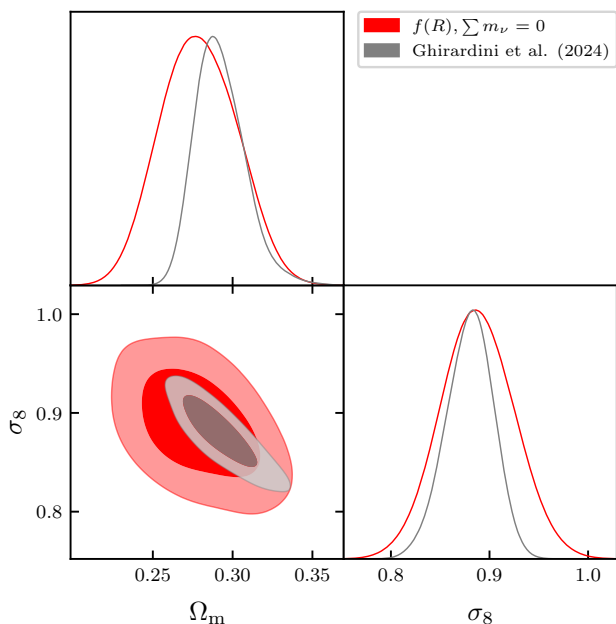


Fig. 3: Comparison of the posteriors obtained on the $\Omega_m - \sigma_8$ plane. We represent the Λ CDM analysis introduced in Ghirardini et al. (A&A subm.) in grey, while the posteriors of HS- $f(R)$ case are shown in red.

The DES, KiDS, and HSC surveys are used simultaneously to calibrate the count rate to mass (Equation 42) and richness to mass (Equation 46) relations. The scatter around this scaling is;

$$\log \sigma_{M_{\text{WL}}}^2 = s(z) + s_M \log \left(\frac{M}{M_p} \right)$$

where the mass component is consistent with zero, and we fix $s_M = 0$ in the rest of the analysis as prescribed by Grandis et al. (A&A subm.).

4.3. Contamination fraction

Although the eRASS1 cosmology subsample is a high-fidelity catalog with a purity level reaching 95%, the remaining 5% contaminants should be eliminated from our analysis. We apply a mixture model fitting for the fraction of AGN and random sources (RS). We refer the reader to (Ghirardini et al. A&A subm.) for a detailed method review.

5. Results

In this section, we provide our results on the HS- $f(R)$ gravity based on cluster counts from the eRASS1 cosmology catalog with weak lensing mass calibration. We first show that our mass scale is consistent with the base Λ CDM analysis from Ghirardini et al. (A&A subm.).

5.1. Comparison of the mass scale with GR- Λ CDM

One of the key ingredients of cluster abundance cosmology is the relation between the observable used to detect the objects and the underlying cluster mass. In this work, the main observable are the X-ray count rates of the clusters observed in the

first eROSITA All-Sky Survey. The modeling of the scaling relations between observable and cluster mass is described in section 4. The parameters of this count rates to mass relation are fitted jointly with the cosmological parameters. This means that when considering extensions to general relativity that do not affect cluster masses due to screening mechanisms, we should find consistent scaling relations, as the fitted cosmology is similar to the one found in Λ CDM.

The redshift dependence of the mass slope C_X is fixed to zero, the luminosity distance dependence D_X to -2, and normalized Hubble parameter dependence E_X to 2. Figure 4 shows the fitted parameters A_X, B_X, F_X and G_X when compared to the standard Λ CDM analysis presented in Ghirardini et al. (A&A subm.) and the weak lensing mass calibration part of the likelihood presented in Grandis et al. (A&A subm.). The latter represents the information coming only from the weak lensing mass calibration of DES clusters.

Overall, there is good agreement between our different models whenever we consider deviation from GR. The mass calibration parameters are indeed not affecting our results. This means that the mass calibration is robust and that changes in the cosmological model primarily affect the underlying distribution of clusters represented by the HMF.

5.2. Constraints on $f(R)$ gravity

We apply two different models to constrain the HS- $f(R)$ gravity parameterization using the Hagstotz et al. (2019) formalism. In the first one, we assume massless neutrinos, while in the second one, we simultaneously constrain the sum of the neutrino masses and the parameter $\log |f_{R0}|$ (Equation (3)). We summarize our results in Table 2. In both cases, eRASS1 cluster number counts provide upper limits on $\log |f_{R0}|$. In the first case, we find the following constraints, summarized in figure 3:

$$\begin{aligned} \Omega_m &= 0.28 \pm 0.02 \\ \sigma_8 &= 0.89 \pm 0.04, \\ S_8 &= 0.85 \pm 0.04 \end{aligned} \quad (49)$$

at 68% confidence level. These constraints are in good agreement with the results of the standard Λ CDM analysis presented in Ghirardini et al. (A&A subm.). Finally, we for the first time obtain constraints on the $f(R)$ parameters with cluster abundance only, obtaining:

$$\log |f_{R0}| < -4.31 \text{ at 95\% confidence } \left(\sum m_\nu = 0 \text{ eV} \right). \quad (50)$$

Figure 6 presents the measurements in the $\Omega_m - \log |f_{R0}|$ plane. Our constraints show consistency with GR, as suggested by previous surveys using cluster abundance to probe HS- $f(R)$ gravity. When combined with CMB data, the most recent study by Cataaneo et al. (2015) obtained $\log |f_{R0}| < -4.79$. Our results suggest that large unscreened departures from GR can be ruled out by cluster counts alone, thus providing an independent test of gravity on scales ~ 10 Mpc. Additionally, Hagstotz et al. (2019) showed that massive neutrinos can counteract the effect of modified gravity by reducing the abundance of massive structures. For instance, massive neutrinos increase the collapse barrier presented in equation 17. For $\sum m_\nu = 0.3$ eV, the collapse barrier is not distinguishable from the GR barrier if $\log |f_{R0}| = -5$. It is thus necessary to investigate the case where the sum of the mass of the neutrinos is fit jointly with $\log |f_{R0}|$. When we free the masses of the neutrinos, we obtain

$$\log |f_{R0}| < -4.12 \text{ at 95\% confidence } \left(\sum m_\nu \text{ free} \right), \quad (51)$$

Table 1: Priors on the cosmological parameters used in this analysis when they are involved in the corresponding model. For the full set of priors used for the other parameters, including scaling relation and nuisance parameters, (see Ghiradini et al. A&A subm.)

Parameter	Units	Description	Prior
Ω_m	-	Mean matter density at present time	$\mathcal{U}(0.2, 0.95)$
$\log A_s$	-	Amplitude of the primordial power spectrum	$\mathcal{U}(-10, -8)$
H_0	$\frac{\text{km}}{\text{s}}/\text{Mpc}$	Hubble expansion rate at present time	$\mathcal{N}(67.77, 0.6)$
Ω_b	-	Mean baryon density at present time	$\mathcal{U}(0.046, 0.052)$
n_s	-	Spectra index of the primordial power spectrum	$\mathcal{U}(0.92, 1.0)$
$\sum m_\nu$	eV	Summed neutrino masses	$\mathcal{U}(0, 1)$
$\log f_{R0} $	-	Logarithm of the derivative of $f(R)$ with respect to the Ricci scalar taken at present day	$\mathcal{U}(-8, -3)$

Notes. With $\mathcal{U}(\text{min}, \text{max})$ we indicate a uniform distribution between ‘min’ and ‘max’. With $\mathcal{N}(\mu, \sigma)$ we indicate a normal distribution centered on μ and with standard deviation σ .

Table 2: Constraints on the HS- $f(R)$ gravity model in different scenarios. The errors provided for the constrained parameters are the 68% confidence intervals. The upper limits are given at the 95% confidence level.

	$\log f_{R0} $	Ω_m	σ_8	$\sum m_\nu$	S_8
HS- $f(R)$	< -5.12	0.28 ± 0.02	0.89 ± 0.04	-	0.85 ± 0.04
HS- $f(R) + \sum m_\nu$	< -4.12	0.29 ± 0.03	0.86 ± 0.05	< 0.39 eV	0.83 ± 0.04

We also the current constraints on the cosmological parameters, including the neutrino masses:

$$\begin{aligned}
\Omega_m &= 0.29 \pm 0.03 \\
\sigma_8 &= 0.86 \pm 0.05 \\
S_8 &= 0.83 \pm 0.04 \\
\sum m_\nu &< 0.44 \text{ eV at } 95\% \text{ confidence}
\end{aligned}
\tag{52}$$

These constraints are again fully consistent with those obtained in the base Λ CDM (Ghiradini et al. A&A subm.) (see table 2). We investigate the consistency between our S_8 measurements and the one given in the standard Λ CDM analysis in Ghiradini et al. (A&A subm.), who finds

$$S_8 = 0.86 \pm 0.01. \tag{53}$$

Figure 5 shows the different models, compared to the results obtained by Planck Collaboration et al. (2020). In all cases, our S_8 value is in good agreement with the cosmic microwave background. Additionally, the three models are fully compatible. However, the upper limits on the neutrino mass are higher due to the increased free parameters in the fits. It is worth noting that we solely use cluster abundances with no priors on the cosmological parameters when constraining f_{R0} . The tighter upper limits reported in the literature, e.g., Kou et al. (2023), find an upper limit of $\log |f_{R0}| < -4.61$, combining the CMB measurements with galaxy clustering. The ability of finding upper limits with cluster counts alone can primarily be explained by the increased statistics provided by the eRASS1 cluster sample. This allows us to provide a self consistent physical framework. Moreover, the constraints benefit from the shear measurement from high-quality DES, KIDS, and HSC mass calibration employed in this work (Grandis et al. A&A subm.; Kleinebreil 2023). It is, therefore, clear that in both cases, whether the neutrino masses are allowed to be free, the constraints from the eRASS1 cluster count measurements remain consistent with GR with a cosmological constant, for which $f_{R0} = 0$ as shown in equation 3.

6. Discussion and conclusions

In this work, we present results on potential deviations from standard GR and Λ CDM using X-ray detected eRASS1 clusters, in combination with LS DR10-South for optical confirmation and redshift measurement, and DES, KiDS, and HSC for weak lensing mass calibration. We derive constraints on the HS model of $f(R)$ gravity. We consider both the case of massive and massless neutrinos.

Overall, all the models that we have studied are statistically consistent with GR. Given the constraining power of eRASS1, we have chosen to present constraints from cluster abundance only. This choice allows us to measure our parameters with a consistent physical framework for the first time. Indeed, this works shows that cluster counts alone have a great potential to constraint modified gravity at the scale at which they are sensitive. Deeper surveys with eROSITA will significantly increase the constraints that we obtain here and might rival the results obtained at smaller scales. Overall, combined with the follow-up weak lensing observations, the first eROSITA’s All-Sky survey has the statistical power to constrain the cosmological parameters with percent level precision and test the general relativity at large scales.

Lastly, we investigate the consistency between our S_8 measurements and the one given in the standard Λ CDM analysis and find good agreement. The modification of gravitation at the scale covered by cluster abundance does not significantly affect the S_8 measurement. Our error bars are increased, but all posteriors are fully compatible. This emphasizes that the S_8 measurement provided in the Λ CDM analysis is robust against modifications and in good agreement with Planck Collaboration et al. (2020).

Finally, the precision of our analysis mostly relies on the halo mass function models available. We use the framework proposed by Hagstotz et al. (2019), while others like Cataneo et al. (2016) propose alternative approaches. Additional work will be necessary to increase the precision of our constraints by increasing the

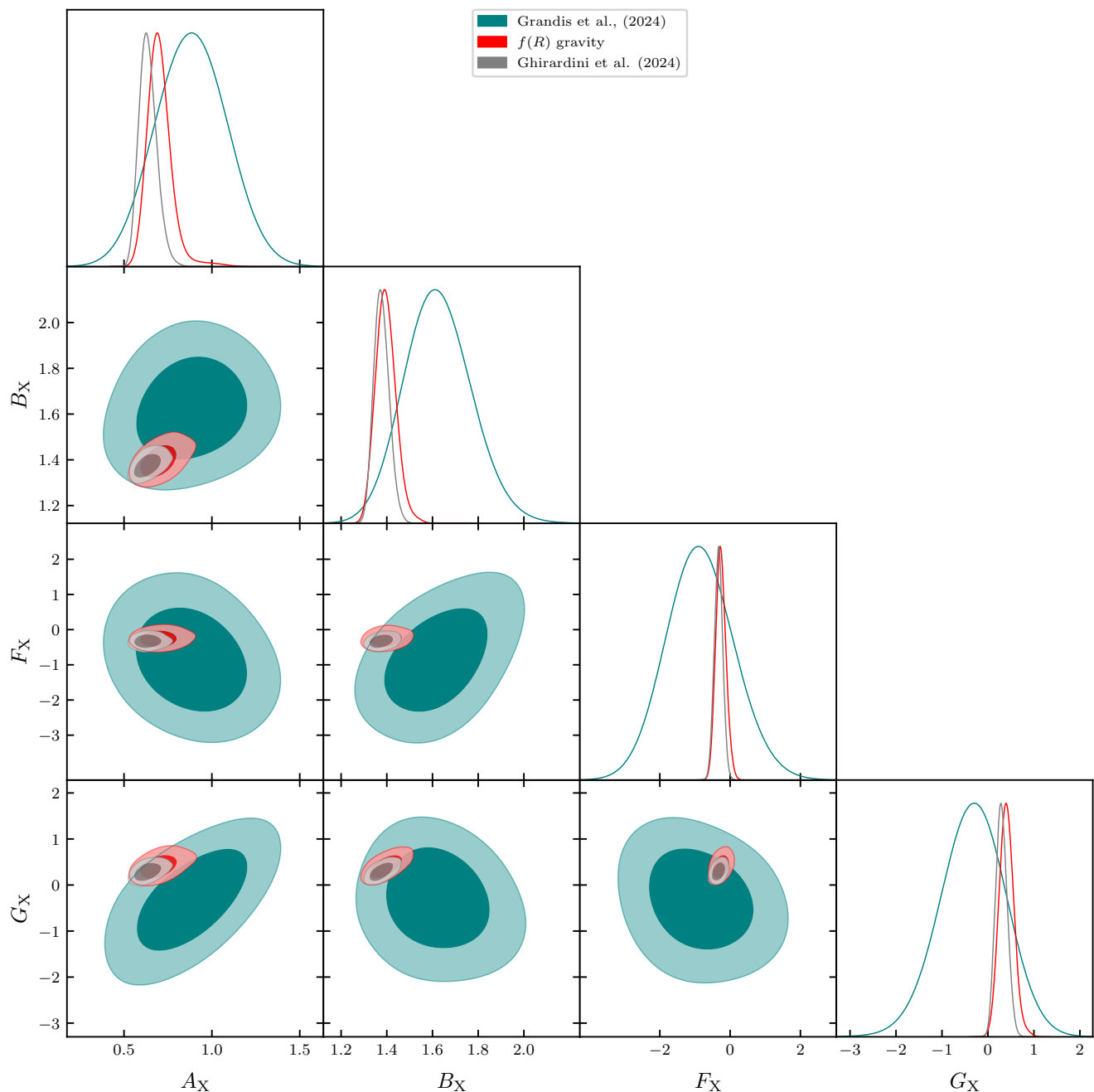


Fig. 4: Comparison of the posteriors on the scaling relation obtained in the $f(R)$ framework (the mass of the neutrinos is fixed) and the standard Λ CDM analysis presented in Ghirardini et al. (A&A *subm.*) (grey). The different models are fully consistent with one another. We overplot the contours obtained from weak lensing only from Grandis et al. (A&A *subm.*).

reliability of the HMF, not only for $f(R)$ gravity, but also for any additional model of interest.

eROSITA, thus far, collected more than four All-Sky survey data. The final eRASS will detect about 10^5 galaxy clusters and groups (projected from the eFEDS results in Liu et al. 2022; Bulbul et al. 2022). The deeper eROSITA data and extensive cluster catalogs, in combination with state-of-the-art weak lensing mass calibration, will allow us to tighten our constraints on the $f(R)$ gravity models.

Acknowledgements. The authors thank Prof. Catherine Heymans for her help and availability for the implementation of the blinding strategy and her useful

comments on the draft. This work is based on data from eROSITA, the soft X-ray instrument aboard SRG, a joint Russian-German science mission supported by the Russian Space Agency (Roskosmos), in the interests of the Russian Academy of Sciences represented by its Space Research Institute (IKI), and the Deutsches Zentrum für Luft und Raumfahrt (DLR). The SRG spacecraft was built by Lavochkin Association (NPOL) and its subcontractors and is operated by NPOL with support from the Max Planck Institute for Extraterrestrial Physics (MPE). The development and construction of the eROSITA X-ray instrument was led by MPE, with contributions from the Dr. Karl Remis Observatory Bamberg & ECAP (FAU Erlangen-Nuernberg), the University of Hamburg Observatory, the Leibniz Institute for Astrophysics Potsdam (AIP), and the Institute for Astronomy and Astrophysics of the University of Tübingen, with the support of DLR and the Max Planck Society. The Argelander Institute for Astronomy of

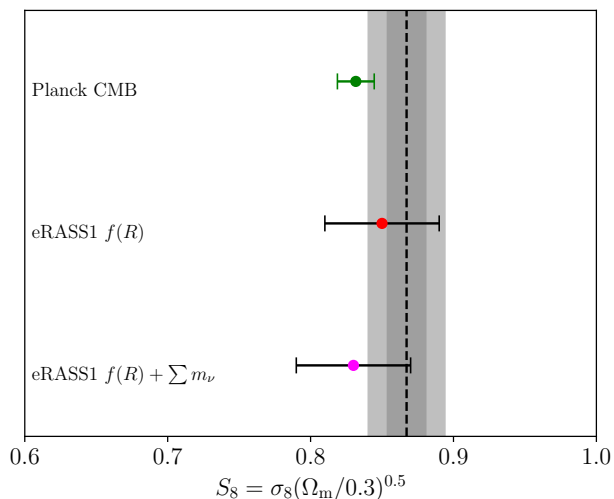


Fig. 5: Comparison of the S_8 parameter obtained using the different models. We show the 1σ uncertainties. The case introducing massless neutrinos is in red, while the one considering massive neutrinos is shown in pink. Results from the cosmic microwave background are shown in green. The grey area represents the 68% and 95% confidence regions of the Λ CDM analysis from Ghirardini et al. (A&A subm.).

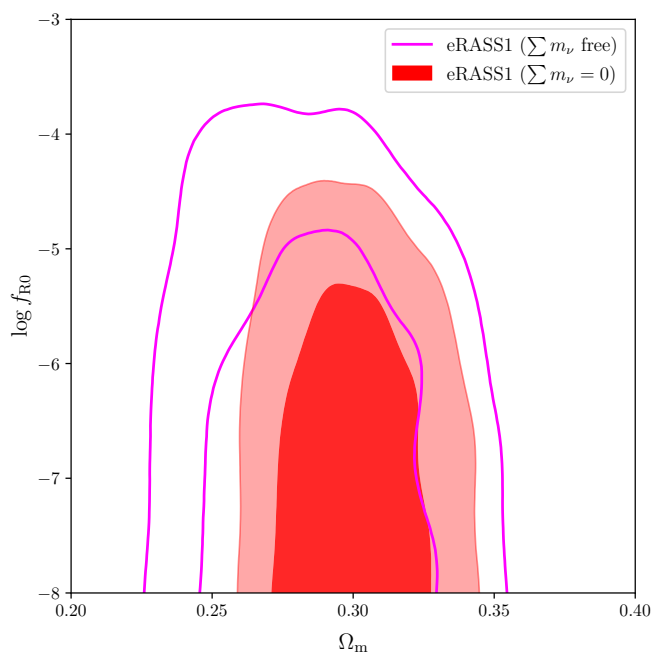


Fig. 6: Constraints obtained on $\log f_{R0}$ with eRASS1 clusters. No external cosmological datasets are combined with our data shown in this figure. Constraints from with fixed neutrino mass are shown in red, while constraints where the neutrino mass is let free is shown in magenta.

the University of Bonn and the Ludwig Maximilians Universität Munich also participated in the science preparation for eROSITA. The eROSITA data shown here were processed using the eSASS software system developed by the German eROSITA consortium.

V. Ghirardini, E. Bulbul, A. Liu, C. Garrel, S. Zelmer, and X. Zhang acknowledge financial support from the European Research Council (ERC) Consolidator Grant under the European Union’s Horizon 2020 research and innovation

program (grant agreement CoG DarkQuest No 101002585). N. Clerc was financially supported by CNES. M. Cataneo acknowledges support from the Alexander von Humboldt Foundation and the German Centre for Cosmological Lensing. T. Schrabback and F. Kleinebreil acknowledge support from the German Federal Ministry for Economic Affairs and Energy (BMWi) provided through DLR under projects 50OR2002, 50OR2106, and 50OR2302, as well as the support provided by the Deutsche Forschungsgemeinschaft (DFG, German Research Foundation) under grant 415537506. The Innsbruck group also acknowledges support provided by the Austrian Research Promotion Agency (FFG) and the Federal Ministry of the Republic of Austria for Climate Action, Environment, Energy, Mobility, Innovation and Technology (BMK) via the Austrian Space Applications Programme with grant numbers 899537 and 900565.

The Legacy Surveys consist of three individual and complementary projects: the Dark Energy Camera Legacy Survey (DECaLS; Proposal ID #2014B-0404; PIs: David Schlegel and Arjun Dey), the Beijing-Arizona Sky Survey (BASS; NOAO Prop. ID #2015A-0801; PIs: Zhou Xu and Xiaohui Fan), and the Mayall z-band Legacy Survey (MzLS; Prop. ID #2016A-0453; PI: Arjun Dey). DECaLS, BASS and MzLS together include data obtained, respectively, at the Blanco telescope, Cerro Tololo Inter-American Observatory, NSF’s NOIRLab; the Bok telescope, Steward Observatory, University of Arizona; and the Mayall telescope, Kitt Peak National Observatory, NOIRLab. Pipeline processing and analyses of the data were supported by NOIRLab and the Lawrence Berkeley National Laboratory (LBNL). The Legacy Surveys project is honored to be permitted to conduct astronomical research on Iolkam Du’ag (Kitt Peak), a mountain with particular significance to the Tohono O’odham Nation.

Funding for the DES Projects has been provided by the U.S. Department of Energy, the U.S. National Science Foundation, the Ministry of Science and Education of Spain, the Science and Technology Facilities Council of the United Kingdom, the Higher Education Funding Council for England, the National Center for Supercomputing Applications at the University of Illinois at Urbana-Champaign, the Kavli Institute of Cosmological Physics at the University of Chicago, the Center for Cosmology and Astro-Particle Physics at the Ohio State University, the Mitchell Institute for Fundamental Physics and Astronomy at Texas A&M University, Financiadora de Estudos e Projetos, Fundação Carlos Chagas Filho de Amparo à Pesquisa do Estado do Rio de Janeiro, Conselho Nacional de Desenvolvimento Científico e Tecnológico and the Ministério da Ciência, Tecnologia e Inovação, the Deutsche Forschungsgemeinschaft, and the Collaborating Institutions in the Dark Energy Survey. The Collaborating Institutions are Argonne National Laboratory, the University of California at Santa Cruz, the University of Cambridge, Centro de Investigaciones Energéticas, Medioambientales y Tecnológicas-Madrid, the University of Chicago, University College London, the DES-Brazil Consortium, the University of Edinburgh, the Eidgenössische Technische Hochschule (ETH) Zürich, Fermi National Accelerator Laboratory, the University of Illinois at Urbana-Champaign, the Institut de Ciències de l’Espai (IEEC/CSIC), the Institut de Física d’Altes Energies, Lawrence Berkeley National Laboratory, the Ludwig-Maximilians Universität München and the associated Excellence Cluster Universe, the University of Michigan, the National Optical Astronomy Observatory, the University of Nottingham, The Ohio State University, the OzDES Membership Consortium, the University of Pennsylvania, the University of Portsmouth, SLAC National Accelerator Laboratory, Stanford University, the University of Sussex, and Texas A&M University. Based on observations made with ESO Telescopes at the La Silla Paranal Observatory under programme IDs 177.A-3016, 177.A-3017, 177.A-3018 and 179.A-2004, and on data products produced by the KiDS consortium. The KiDS production team acknowledges support from: Deutsche Forschungsgemeinschaft, ERC, NOVA and NWO-M grants; Target; the University of Padova, and the University Federico II (Naples). This paper makes use of software developed for the Large Synoptic Survey Telescope. We thank the LSST Project for making their code available as free software at <http://dm.lsst.org>

This work made use of the following Python software packages: SciPy¹ (Virtanen et al. 2020), Matplotlib² (Hunter 2007), Astropy³ (Astropy Collaboration et al. 2022), NumPy⁴ (Harris et al. 2020), CAMB (Lewis & Challinor 2011), pyCCL⁵ (Chisari et al. 2019), GPy⁶ (GPy since 2012), climin⁷ (Bayer et al. 2015), ultranest⁸ (Buchner 2021)

¹ <https://scipy.org/>

² <https://matplotlib.org/>

³ <https://www.astropy.org/>

⁴ <https://numpy.org/>

⁵ <https://github.com/LSSTDESC/CCL>

⁶ <https://github.com/SheffieldML/GPy>

⁷ <https://github.com/BRML/climin>

⁸ <https://github.com/JohannesBuchner/UltraNest/>

References

- Aihara, H., Armstrong, R., Bickerton, S., et al. 2018, PASJ, 70, S8
- Alam, S., Ata, M., Bailey, S., et al. 2017, MNRAS, 470, 2617
- Amon, A., Gruen, D., Troxel, M. A., et al. 2022, Phys. Rev. D, 105, 023514
- Artis, E., Melin, J.-B., Bartlett, J. G., & Murray, C. 2021, A&A, 649, A47
- Asgari, M., Lin, C.-A., Joachimi, B., et al. 2021, A&A, 645, A104
- Astropy Collaboration, Price-Whelan, A. M., Lim, P. L., et al. 2022, ApJ, 935, 167
- Bartelmann, M. & Schneider, P. 2001, Phys. Rep., 340, 291
- Bayer, J., Osendorfer, C., Diot-Girard, S., Rueckstiehs, T., & Urban, S. 2015, TUM, Tech. Rep.
- Bekenstein, J. D. & Sanders, R. H. 1994, ApJ, 429, 480
- Bennett, C. L., Larson, D., Weiland, J. L., et al. 2013, ApJS, 208, 20
- Bocquet, S., Dietrich, J. P., Schrabback, T., et al. 2019, ApJ, 878, 55
- Bocquet, S., Grandis, S., Bleem, L. E., et al. 2023, arXiv e-prints, arXiv:2310.12213
- Bocquet, S., Grandis, S., Bleem, L. E., et al. 2024, arXiv e-prints, arXiv:2401.02075
- Bocquet, S., Heitmann, K., Habib, S., et al. 2020, ApJ, 901, 5
- Bocquet, S., Saro, A., Mohr, J. J., et al. 2015, ApJ, 799, 214
- Buchner, J. 2021, The Journal of Open Source Software, 6, 3001
- Bulbul, E., Liu, A., Kluge, M., & et al. A&A subm.
- Bulbul, E., Liu, A., Pasini, T., et al. 2022, A&A, 661, A10
- Cataneo, M., Rapetti, D., Lombriser, L., & Li, B. 2016, J. Cosmology Astropart. Phys., 2016, 024
- Cataneo, M., Rapetti, D., Schmidt, F., et al. 2015, Phys. Rev. D, 92, 044009
- Chisari, N. E., Alonso, D., Krause, E., et al. 2019, CCL: Core Cosmology Library, Astrophysics Source Code Library, record ascl:1901.003
- Clerc, N. & Finoguenov, A. 2023, in Handbook of X-ray and Gamma-ray Astrophysics. Edited by Cosimo Bambi and Andrea Santangelo, 123
- Clerc, N. e. a. 2023
- Costanzi, M., Rozo, E., Simet, M., et al. 2019, MNRAS, 488, 4779
- De Felice, A. & Tsujikawa, S. 2010, Living Reviews in Relativity, 13, 3
- Despali, G., Giocoli, C., Angulo, R. E., et al. 2016, MNRAS, 456, 2486
- Duffy, A. R., Schaye, J., Kay, S. T., & Dalla Vecchia, C. 2008, MNRAS, 390, L64
- Eisenstein, D. J., Zehavi, I., Hogg, D. W., et al. 2005, ApJ, 633, 560
- Euclid Collaboration, Castro, T., Fumagalli, A., et al. 2023a, A&A, 671, A100
- Euclid Collaboration, Giocoli, C., Meneghetti, M., et al. 2023b, arXiv e-prints, arXiv:2302.00687
- Freedman, W. L., Madore, B. F., Hatt, D., et al. 2019, ApJ, 882, 34
- Fumagalli, A., Costanzi, M., Saro, A., Castro, T., & Borgani, S. 2023, arXiv e-prints, arXiv:2310.09146
- Gannouji, R., Moraes, B., & Polarski, D. 2009, J. Cosmology Astropart. Phys., 2009, 034
- Garrel, C., Bulbul, E., Ghirardini, V., & et al. in prep.
- Garrel, C., Pierre, M., Valageas, P., et al. 2022, A&A, 663, A3
- Gatti, M., Sheldon, E., Amon, A., et al. 2021, MNRAS, 504, 4312
- Ghirardini, V., Bulbul, E., Artis, E., et al. A&A subm.
- Giblin, B., Heymans, C., Asgari, M., et al. 2021, A&A, 645, A105
- Giocoli, C., Baldi, M., & Moscardini, L. 2018, MNRAS, 481, 2813
- GPY. since 2012, GPY: A Gaussian process framework in python, <http://github.com/SheffieldML/GPY>
- Grandis, S., Bocquet, S., Mohr, J. J., Klein, M., & Dolag, K. 2021a, MNRAS, 507, 5671
- Grandis, S., Ghirardini, E., & et al. A&A subm.
- Grandis, S., Mohr, J. J., Costanzi, M., et al. 2021b, MNRAS, 504, 1253
- Gupta, S., Hellwing, W. A., Bilicki, M., & García-Farieta, J. E. 2022, Phys. Rev. D, 105, 043538
- Hagstotz, S., Costanzi, M., Baldi, M., & Weller, J. 2019, MNRAS, 486, 3927
- Harris, C. R., Millman, K. J., van der Walt, S. J., et al. 2020, Nature, 585, 357
- Hildebrandt, H., van den Busch, J. L., Wright, A. H., et al. 2021, A&A, 647, A124
- Hu, B., Raveri, M., Frusciante, N., & Silvestri, A. 2014, Phys. Rev. D, 89, 103530
- Hu, W. & Kravtsov, A. V. 2003, ApJ, 584, 702
- Hu, W. & Sawicki, I. 2007, Phys. Rev. D, 76, 064004
- Huff, E. & Mandelbaum, R. 2017, arXiv e-prints, arXiv:1702.02600
- Hunter, J. D. 2007, Computing in Science & Engineering, 9, 90
- Ider Chitham, J., Comparat, J., Finoguenov, A., et al. 2020, MNRAS, 499, 4768
- Khouri, J. & Weltman, A. 2004, Phys. Rev. D, 69, 044026
- Kleinebreil, F. e. a. 2023
- Kluge, M., Comparat, J., Balzer, M., & et al. A&A subm.
- Knebe, A., Pearce, F. R., Lux, H., et al. 2013, MNRAS, 435, 1618
- Kopp, M., Appleby, S. A., Achitouv, I., & Weller, J. 2013, Phys. Rev. D, 88, 084015
- Kou, R., Murray, C., & Bartlett, J. G. 2023, arXiv e-prints, arXiv:2311.09936
- Kuijken, K., Heymans, C., Dvornik, A., et al. 2019, A&A, 625, A2
- Lacasa, F. & Grain, J. 2019, A&A, 624, A61
- Lesci, G. F., Nanni, L., Marulli, F., et al. 2022, A&A, 665, A100
- Lesgourgues, J. 2011, arXiv e-prints, arXiv:1104.2932
- Lewis, A. & Challinor, A. 2011, CAMB: Code for Anisotropies in the Microwave Background, Astrophysics Source Code Library, record ascl:1102.026
- Li, B., Zhao, G.-B., & Koyama, K. 2012, MNRAS, 421, 3481
- Li, X., Miyatake, H., Luo, W., et al. 2022, PASJ, 74, 421
- Li, X., Zhang, T., Sugiyama, S., et al. 2023, arXiv e-prints, arXiv:2304.00702
- Liu, A., Bulbul, E., Ghirardini, V., et al. 2022, A&A, 661, A2
- Lombriser, L., Li, B., Koyama, K., & Zhao, G.-B. 2013, Phys. Rev. D, 87, 123511
- Lombriser, L., Slosar, A., Seljak, U., & Hu, W. 2012, Phys. Rev. D, 85, 124038
- Mantz, A. B., von der Linden, A., Allen, S. W., et al. 2015, MNRAS, 446, 2205
- Merloni, A., Lamer, G., Liu, T., et al. 2024, arXiv e-prints, arXiv:2401.17274
- Mitchell, M. A., He, J.-h., Arnold, C., & Li, B. 2018, MNRAS, 477, 1133
- Nakamura, T. T. & Suto, Y. 1997, Progress of Theoretical Physics, 97, 49
- Navarro, J. F., Frenk, C. S., & White, S. D. M. 1996, ApJ, 462, 563
- Oyaizu, H. 2008, Phys. Rev. D, 78, 123523
- Percival, W. J. & White, M. 2009, MNRAS, 393, 297
- Perlmutter, S., Aldering, G., Goldhaber, G., et al. 1999, ApJ, 517, 565
- Planck Collaboration, Aghanim, N., Akrami, Y., et al. 2020, A&A, 641, A6
- Preston, C., Amon, A., & Efsthathiou, G. 2023, MNRAS, 525, 5554
- Riess, A. G., Casertano, S., Yuan, W., Macri, L. M., & Scolnic, D. 2019, ApJ, 876, 85
- Riess, A. G., Filippenko, A. V., Challis, P., et al. 1998, AJ, 116, 1009
- Ruan, C.-Z., Cuesta-Lazaro, C., Eggemeier, A., et al. 2023, arXiv e-prints, arXiv:2301.02970
- Salvati, L., Douspis, M., & Aghanim, N. 2020, A&A, 643, A20
- Sanders, J. S., Fabian, A. C., Russell, H. R., & Walker, S. A. 2018, MNRAS, 474, 1065
- Schmidt, F. 2010, Phys. Rev. D, 81, 103002
- Schmidt, F., Vikhlinin, A., & Hu, W. 2009, Phys. Rev. D, 80, 083505
- Seppi, R., Comparat, J., Ghirardini, V., & et al. A&A subm.
- Sheldon, E. S. & Huff, E. M. 2017, ApJ, 841, 24
- Sunayama, T., Miyatake, H., Sugiyama, S., et al. 2023, arXiv e-prints, arXiv:2309.13025
- Tinker, J., Kravtsov, A. V., Klypin, A., et al. 2008, ApJ, 688, 709
- Troxel, M. A., MacCrann, N., Zuntz, J., et al. 2018, Phys. Rev. D, 98, 043528
- Tsujikawa, S., Gannouji, R., Moraes, B., & Polarski, D. 2009, Phys. Rev. D, 80, 084044
- Vikhlinin, A., Burenin, R. A., Ebeling, H., et al. 2009, ApJ, 692, 1033
- Virtanen, P., Gommers, R., Oliphant, T. E., et al. 2020, Nature Methods, 17, 261
- von Braun-Bates, F., Winther, H. A., Alonso, D., & Devriendt, J. 2017, J. Cosmology Astropart. Phys., 2017, 012
- Wang, Z., Mirpoorian, S. H., Pogossian, L., Silvestri, A., & Zhao, G.-B. 2023, J. Cosmology Astropart. Phys., 2023, 038
- Wolf, W. J. & Ferreira, P. G. 2023, arXiv e-prints, arXiv:2310.07482
- Wright, A. H., Hildebrandt, H., van den Busch, J. L., & Heymans, C. 2020, A&A, 637, A100
- Wright, C. O. & Brainerd, T. G. 2000, ApJ, 534, 34
- Xu, L. 2015, arXiv e-prints, arXiv:1506.03232
- Zhao, G.-B., Li, B., & Koyama, K. 2011, Phys. Rev. D, 83, 044007
- Zubeldia, Í. & Challinor, A. 2019, MNRAS, 489, 401
- Zucca, A., Pogossian, L., Silvestri, A., & Zhao, G. B. 2019, J. Cosmology Astropart. Phys., 2019, 001
- Zumalacárregui, M., Bellini, E., Sawicki, I., Lesgourgues, J., & Ferreira, P. G. 2017, J. Cosmology Astropart. Phys., 2017, 019